TIV Contrast Source Inversion of mCSEM data

Torgeir Wiik[*], **Lars Ole Løseth**[†], **Bjørn Ursin**[*] **and Ketil Hokstad**[*,†]

[*]*Norwegian University of Science and Technology,*

Department for Petroleum Engineering and Applied Geophysics,

S.P. Andersens vei 15A,

NO-7491 Trondheim, Norway

torgeir.wiik@ntnu.no

bjorn.ursin@ntnu.no

[†]*Statoil Research Center,*

Arkitelt Ebbells veg 10,

NO-7053 Ranheim, Norway

lalo@statoil.com

kehok@statoil.com

(August 28, 2010)

1

Running head: **TIV Contrast Source Inversion**

ABSTRACT

We present a 3D Contrast Source Inversion (CSI) scheme for electromagnetic data in conductive media. We consider only contrasts in electric conductivity, but allow the medium to be transversely isotropic in the vertical direction (TIV). This has applications for instance in inversion of marine Controlled Source Electromagnetic data. The CSI method is based on the integral equation formulation of electromagnetic field propagation, and we show how the method solves the inverse problem of determining the conductivity structure of the subsurface. The method minimizes a cost functional which enforces data fidelity and that the solution should satisfy the Lippmann-Schwinger equation. Further regularization is introduced linearly into the cost functional to incorporate prior model information. Although the problem is non-linear we choose a strategy of splitting the minimization problem into two linear problems, which are solved alternatingly. To this end contrast sources are introduced, which may be interpreted as sources emitting the scattered field from a scattering object. Two synthetic and two real field examples are inverted, which demonstrate the method and how the TIV inversion performs compared to isotropic inversion. We find that the CSI method is applicable to real field examples, and the results show that a TIV inversion is preferred over isotropic in order to identify weak anomalies in these examples. The reason for this is that both the horizontal and vertical conductivity affects the signal propagation in the overburden.

INTRODUCTION

The use of marine Controlled Source Electromagnetic (mCSEM) data in hydrocarbon prospecting is based on the assumption that hydrocarbon saturated formations possess a significantly lower electric conductivity compared to its surroundings. The EM field emitted from a controlled source travelling inside this resistive region will be less attenuated at far source/receiver offsets than the field propagating in water saturated formations, and the effect of such resistive areas should thus be recognizable at far offsets (Eidesmo et al., 2002). The mCSEM experiment is usually performed by towing a horizontal electric dipole behind a vessel. The dipole typically outputs a binary waveform which is the source of electromagnetic signals in the frequency range 0.1Hz-10Hz. The emitted field travels in the subsurface, before it is recorded when it reaches the seabed (Eidesmo et al., 2002). However, interpretation of mCSEM is not necessarily straightforward. In order to explain the recorded data, imaging algorithms that solves the inverse scattering problem of determining the subsurface parameters are helpful.

EM inverse scattering is a classical topic and has been investigated earlier, see for instance Colton and Kress (1992). In particular, solving both the forward and inverse scattering problem has attracted increased interest from the geophysical society in the later years, treating both crosswell and mCSEM experiments. See for instance Ursin (1983); Wannamaker et al. (1984); Ward and Hohmann (1987); Løseth and Ursin (2007); Kong et al. (2008); Abubakar et al. (2008a) for modeling, and Newman (1995); Abubakar and van den Berg (1998, 2000); Newman and Hoversten (2000); Zhdanov

(2002); Abubakar et al. (2008a); Newman et al. (2010) for inversion. However, mostly isotropic inversion is considered.

We wish to apply the so called 3D Contrast Source Inversion (CSI) method, extended to media which are transversely isotropic in the vertical direction (TIV), in the mCSEM setting. This means considering media in which the horizontal and vertical conductivities may differ. Anisotropic effects are present in recorded data and hence the isotropic assumption may not be sufficient. The isotropic method has been investigated in several other settings earlier, see for instance van den Berg and Kleinman (1997); Abubakar and van den Berg (2002); Abubakar et al. (2002), where the latter concerns high frequency medical imaging.

The novel work in this paper includes the application of an anisotropic version of the CSI algorithm to the low frequency, diffusive fields in mCSEM applications. We use the integral equation framework described earlier by e.g. Wannamaker et al. (1984); de Hoop (1995); Zhdanov (2002); Abubakar and van den Berg (2004), but the method has also been explored using finite differences (Abubakar et al., 2008b). The method introduces so called *contrast sources*, which appear due to a conductivity contrast, or relative difference, compared to a chosen background. The contrast sources can be interpreted as sources emitting the scattered signals from an anomalous object. The CSI method is thus equivalent to inverting for anomalous currents due to the conductivity contrast. Based on these contrast sources we alternatingly minimize a cost functional with respect to the contrast sources and the contrast between the real medium and a chosen background medium, respectively. The final goal is to obtain an estimate of the contrast which describes the difference between the chosen background and the estimated medium. Thus, the contrast sources are only needed as intermediate values.

Solving the electromagnetic inverse problem is a notoriously ill-posed problem (Zhdanov, 2002; Feng et al., 2003; Abubakar et al., 2004) in the Hadamard sense (McOwen, 1996). By this we mean that that the problem might not depend continuously on the initial conditions and that there exists several solutions. Hence, there is a need for regularization to enforce a physically meaningful solution. Such regularization may be introduced in several ways, for instance multiplicatively into the cost functional as described by Abubakar and van den Berg (2004), or linearly (Tikhonov and Arsenin, 1977). We will here introduce a regularizer linearly into the cost functional, which enforces the contrast estimate to remain close to a reference model in some sense, described by weights. We use weights corresponding to a second order smoothing filter and a zero reference model, thus emphasizing the smoothness of the reconstruction, in order to stabilize the numerical calculations. The weights may also be specified, as described later, to incorporate prior model information. This has, to our knowledge, not been done with the integral equation CSI method earlier.

This method is of interest for mCSEM applications because due to the nature of the integral equation framework only a relatively small subdomain needs to be treated if a suitable bakground model can be chosen, compared to finite difference and finite elements methods which treat the entire subsurface. Together with the approximation of the non-linear problem by two linear problems, which is due to the alternating algorithm, this yields an algorithm which in such cases has small memory requirements and can be run relatively fast due to the small domain considered. In mCSEM prospecting, where typically an entire suite of models need to be investigated, the characteristics of this method should prove useful.

We apply the CSI method to two synthetic and two real field examples. The results show the importance of including anisotropy in the inversion and of considering the information content in the recorded data and the regularizer's nature before performing an inversion. We find that the CSI method is applicable to real field examples, and in these examples a TIV inversion is preferred over isotropic in order to identify weak anomalies. This is because both the horizontal and vertical conductivities affect the field propagation in the overburden (Løseth, 2007).

THEORY

Forward scattering

Consider a background medium described by its electromagnetic parameters

$$\boldsymbol{\sigma}_0 = \begin{pmatrix} \sigma_{0,h} & 0 & 0 \\ 0 & \sigma_{0,h} & 0 \\ 0 & 0 & \sigma_{0,v} \end{pmatrix} = \sigma_{0,v} \begin{pmatrix} \Upsilon & 0 & 0 \\ 0 & \Upsilon & 0 \\ 0 & 0 & 1 \end{pmatrix}, \tag{1}$$

$\boldsymbol{\epsilon}_0 = \epsilon_0 \mathbf{I}$ and $\boldsymbol{\mu}_0 = \mu_0 \mathbf{I}$, where $\mathbf{I}$ is the identity tensor. Here $\sigma_{0,h}$ and $\sigma_{0,v}$ denote the vertical and horizontal conductivities, which may differ in a TIV medium. These parameters are assumed to have some spatial dependence. We accept Ohm's law, which states (Stratton, 1941)

$$\mathbf{j} = \boldsymbol{\sigma}\mathbf{e}, \tag{2}$$

where $\mathbf{e}$ is the electric field. The electric and magnetic field satisfies Maxwell's equations, which in the frequency domain then read (Stratton, 1941)

$$\begin{aligned} \nabla \times \mathbf{e} &= \mathrm{i}\omega\mu_0\mathbf{h}, & (3) \\ \nabla \times \mathbf{h} &= \tilde{\boldsymbol{\sigma}}_0\mathbf{e} + \mathbf{j}^{\mathrm{s}}. & (4) \end{aligned}$$

where $\tilde{\boldsymbol{\sigma}}_0 = \boldsymbol{\sigma}_0 - \mathrm{i}\omega\epsilon_0\mathbf{I}$ and $\mathbf{j}^{\mathrm{s}}$ is the electric source current. Here $\mathrm{i} = \sqrt{-1}$ and ω denotes the angular frequency.

Green's tensors generalizes the concept of Green's functions for scalar equations to vector valued equations (Green, 1828; McOwen, 1996). Physically they represent fields from a point source, and the Green's tensors in 3 dimensions are thus represented by 3×3-matrices with element (i, j) representing the field in i-direction from a point source polarized in the j-direction, $i, j \in \{x, y, z\}$ (or some other basis for $\mathbb{R}^3$). This implies that the electric and magnetic Green's tensors due to an electric point source are solutions of the equations

$$\begin{aligned} \nabla \times \mathbf{G}^E(\mathbf{x}, \mathbf{x_0}) &= \mathrm{i}\omega\mu_0\mathbf{G}^H(\mathbf{x}, \mathbf{x_0}), & (5) \\ \nabla \times \mathbf{G}^H(\mathbf{x}, \mathbf{x_0}) &= \tilde{\sigma_{\mathbf{0}}}\mathbf{G}^E(\mathbf{x}, \mathbf{x_0}) + \mathbf{I}\delta(\mathbf{x} - \mathbf{x_0}), & (6) \end{aligned}$$

where $\mathbf{G}^E$ and $\mathbf{G}^H$ are the electric and magnetic Green's tensors, respectively, $\nabla\times$ is the dyadic operator corresponding to the well-known vector-curl operator, δ is Dirac's delta function and $\mathbf{x_0}$ is the source position.

The solution to equations 3 and 4 for some external, electric source with current-signature $\mathbf{j}^{\mathrm{s}}$ is then given component wise by (Zhdanov, 2002)

$$e_i(\mathbf{x}) = \int_{\mathbb{R}^3} G^E_{ij}(\mathbf{x},\mathbf{x}')j^{\mathrm{s}}_j(\mathbf{x}')\mathrm{d}\mathbf{x}', \tag{7}$$

$$h_i(\mathbf{x}) = \int_{\mathbb{R}^3} G^H_{ij}(\mathbf{x},\mathbf{x}')j^{\mathrm{s}}_j(\mathbf{x}')\mathrm{d}\mathbf{x}'. \tag{8}$$

We have here adopted Einstein's convention of sums and $i, j \in \{x, y, z\}$ denotes the component of the vectors and tensors. Equations 7 and 8 together show how to model electromagnetic fields in a background model with known Green's tensors, due to an electric source.

Consider now a background model $\mathcal{B}$ with given parameters, $\sigma_{\mathbf{0}}, \epsilon_0, \mu_0$, as described above, and assume there in $\mathcal{B}$ is a domain $\mathcal{D}$ of finite volume which contains an inhomogeneity, or anomaly, compared to the electric conductivity, σ, of the background model. In our setting, the inhomogeneity in $\mathcal{D}$ might represent the hydrocarbon reservoir. Assume $\mathcal{D}$ is illuminated by an electric source from the outside, and on a domain $\mathcal{S}$ outside $\mathcal{D}$ receivers record the scattered field due to the conductivity contrast. In Figure 1 an intersection in the xz-plane of the model described is displayed. Now, from equations 7 and 8 we can calculate the incident electric and magnetic field in the domain $\mathcal{D}$ due to an electric source, e^{inc}_i and h^{inc}_i, respectively.

We denote the conductivity inside $\mathcal{D}$ by σ. It is well known that in $\mathcal{D}$ the electric field satisfies (de Hoop, 1995; Abubakar and van den Berg, 2004)

$$e_i\left(\mathbf{x}\right) = e^{\mathrm{inc}}_i\left(\mathbf{x}\right) + \int_{\mathcal{D}} G^E_{ij}\left(\mathbf{x},\mathbf{x}'\right)\sigma_{0,v}\left(\mathbf{x}'\right)\chi_{jj}\left(\mathbf{x}'\right)e_j\left(\mathbf{x}'\right)\mathrm{d}\mathbf{x}', \quad \mathbf{x}\in\mathcal{D}, \tag{9}$$

which is the equivalent to the Lippmann-Schwinger equation for the scalar Helmholtz equation (Colton and Kress, 1992). Here $e_i^{\mathrm{inc}}(\mathbf{x})$ represents the incident electric field from the source, while the integral term represents the scattered field. The contrast $\boldsymbol{\chi}$ is given by

$$\boldsymbol{\chi} = \begin{pmatrix} \chi_h & 0 & 0 \\ 0 & \chi_h & 0 \\ 0 & 0 & \chi_v \end{pmatrix}, \tag{10}$$

where $\chi_h = \frac{\sigma_h}{\sigma_{0,v}} - \Upsilon$ and $\chi_v = \frac{\sigma_v}{\sigma_{0,v}} - 1$. When the total electric field inside $\mathcal{D}$ is established we may calculate the scattered field at receiver locations by (Abubakar and van den Berg, 2004)

$$f_i^E(\mathbf{x}) = \int_{\mathcal{D}} G_{ij}^E(\mathbf{x},\mathbf{x}')\,\sigma_{0,v}(\mathbf{x}')\,\chi_{jj}(\mathbf{x}')\,e_j(\mathbf{x}')\,\mathrm{d}\mathbf{x}', \quad \mathbf{x} \in \mathcal{S}, \tag{11}$$

$$f_i^H(\mathbf{x}) = \int_{\mathcal{D}} G_{ij}^H(\mathbf{x},\mathbf{x}')\,\sigma_{0,v}(\mathbf{x}')\,\chi_{jj}(\mathbf{x}')\,e_j(\mathbf{x}')\,\mathrm{d}\mathbf{x}', \quad \mathbf{x} \in \mathcal{S}. \tag{12}$$

Thus, if we know the Green's tensors of the background medium we can model the scattered field from the inhomogeneity at a receiver location using equations 9-12.

For simplicity we introduce the vectors $\mathbf{e} = (e_x, e_y, e_z)^T$, $\mathbf{f}^E = \left(f_x^E, f_y^E, f_z^E\right)^T$ and $\mathbf{f}^H = \left(f_x^H, f_y^H, f_z^H\right)^T$ and rewrite equations 9-12 in operator form

$$\mathbf{e} = \mathbf{e}^{\mathrm{inc}} + G^{E,\mathcal{D}}\boldsymbol{\chi}\mathbf{e}, \tag{13}$$

$$\mathbf{f}^E = G^{E,\mathcal{S}}\boldsymbol{\chi}\mathbf{e}, \tag{14}$$

$$\mathbf{f}^H = G^{H,\mathcal{S}}\boldsymbol{\chi}\mathbf{e}, \tag{15}$$

where now $G^{E,\mathcal{D}}, G^{E,\mathcal{S}}, G^{H,\mathcal{S}}$ are integral operators.

Contrast Source Inversion

We now wish to solve the inverse problem of estimating $\boldsymbol{\chi}$ inside $\mathcal{D}$ given the scattered fields, that is to determine the conductivity profile of $\mathcal{D}$. We introduce the set of contrast sources, which are anomalous currents normalized by the background conductivity, defined as (Abubakar et al., 2004)

$$\mathcal{W} = \left\{\mathbf{w}^{j,k}\right\}_{j=1\ldots N_s}^{k=1\ldots N_f} = \left\{\boldsymbol{\chi}\mathbf{e}^{j,k}\right\}_{j=1\ldots N_s}^{k=1\ldots N_f}, \tag{16}$$

where N_s is the total number of sources and N_f is the number of frequencies. Introducing this into equations 13-15 yields for a given source and frequency

$$\begin{aligned}
\mathbf{e} &= \mathbf{e}^{\text{inc}} + G^{E,\mathcal{D}}\mathbf{w}, &(17)\\
\mathbf{f}^{E} &= G^{E,\mathcal{S}}\mathbf{w}, &(18)\\
\mathbf{f}^{H} &= G^{H,\mathcal{S}}\mathbf{w}. &(19)
\end{aligned}$$

We will from now use a norm similar to that associated with $L^2(\mathrm{A})$, where $\mathrm{A} \subset \mathbb{R}^3$ is some domain, which is given by

$$\|f\|_{\mathrm{A}}^2 = \int_{\mathrm{A}} |f(\mathbf{x})|^2 \, \mathrm{d}\mathbf{x}. \tag{20}$$

For more information on the norms, confer to Abubakar and van den Berg (2004).

The contrast source inversion (CSI) problem is formulated as a minimization problem as follows (Abubakar and van den Berg, 2004):

Find the contrast χ*, and the set of contrast sources* $\mathcal{W} = \left\{\mathbf{w}^{j,k}\right\}_{j=1\ldots N_\mathrm{s}}^{k=1\ldots N_\mathrm{f}}$*, such that* *the cost functional*

$$
\begin{aligned}
F_1(\mathcal{W},\boldsymbol{\chi}) &= \alpha_1^E \sum_{k=1}^{N_\mathrm{f}} \sum_{j=1}^{N_\mathrm{s}} \left\| \Xi^{E,j,k} \left(\mathbf{f}^{E,j,k} - G^{E,\mathcal{S},k} \mathbf{w}^{j,k} \right) \right\|_{\mathcal{S}}^2 \\
&+ \alpha_1^H \sum_{k=1}^{N_\mathrm{f}} \sum_{j=1}^{N_\mathrm{s}} \left\| \Xi^{H,j,k} \left(\mathbf{f}^{H,j,k} - G^{H,\mathcal{S},k} \mathbf{w}^{j,k} \right) \right\|_{\mathcal{S}}^2 \qquad (21) \\
&+ \alpha_2 \sum_{k=1}^{N_\mathrm{f}} \sum_{j=1}^{N_\mathrm{s}} \left\| \boldsymbol{\chi} \mathbf{e}^{\mathrm{inc},j,k} - \mathbf{w}^{j,k} + \boldsymbol{\chi} G^{E,\mathcal{D},k} \mathbf{w}^{j,k} \right\|_{\mathcal{D}}^2
\end{aligned}
$$

is minimized.

In this formulation, the two first terms encourage data fidelity, while the last term encourages the solution to solve equation 17. This last term may be viewed as a physical regularization (Abubakar and van den Berg, 2004). Here $\alpha_1^E, \alpha_1^H, \alpha_2$ are normalization factors with reciprocals given by

$$
\begin{aligned}
\alpha_1^{E^{-1}} &= \sum_{k=1}^{N_\mathrm{f}} \sum_{j=1}^{N_\mathrm{s}} \left\| \Xi^{E,j,k} \mathbf{f}^{E,j,k} \right\|_{\mathcal{S}}^2, \qquad (22) \\
\alpha_1^{H^{-1}} &= \sum_{k=1}^{N_\mathrm{f}} \sum_{j=1}^{N_\mathrm{s}} \left\| \Xi^{H,j,k} \mathbf{f}^{H,j,k} \right\|_{\mathcal{S}}^2, \qquad (23) \\
\alpha_2^{-1} &= \sum_{k=1}^{N_\mathrm{f}} \sum_{j=1}^{N_\mathrm{s}} \left\| \boldsymbol{\chi} \mathbf{e}^{\mathrm{inc},j,k} \right\|_{\mathcal{D}}^2, \qquad (24)
\end{aligned}
$$

and Ξ are data weights. The data weights may be chosen e.g. as window functions to remove unwanted noisy areas in the data or to emphasize some offset ranges. In our real data examples, the prior choice has been applied to small ($\leq$ 1000m) and large ($\geq$ 10000m) offsets, and at particularly noisy data. This is performed by assigning particularly low weights to these datapoints such that they have no influence on the inversion. The latter choice may be preferred in more complex cases where data from some offsets are considered more important than others.

To solve the CSI problem we follow Abubakar and van den Berg (2004); Abubakar et al. (2004) and use the following iterative, alternating scheme, which approximates the full non linear problem by two linear problems:

```
Input: Initial contrast and contrast sources
foreach iteration do
    foreach frequency do
        foreach source do
            Minimize equation 21 with respect to $\mathbf{w}^{j,k}$
        end
    end
    Minimize equation 21 with respect to $\chi$
    if stop criterion is true then
        stop iterations
    else
        proceed to next iteration
    end
end
```

Several stopping criterions can be used, for instance one that stops after a sufficient data fit is reached. We stop the iterations if the relative difference between the values of the costfunctional at two subsequent iterations is below a user specified threshold.

We will from now denote $\mathbf{w}^{(n),j,k}$ and $\boldsymbol{\chi}^{(n)}$ as the estimates for the contrast sources and the contrast after iteration n. For the minimization with respect to the contrast sources, we follow Abubakar and van den Berg (2004) and use a conjugate gradient

(CG) method as described by van den Berg (1984). In each iteration we do one CG step to the Euler-Lagrange equation for the contrast source j, k:

$$\begin{aligned}\Big[\alpha_1^E \left(\Xi^{E,j,k} G^{E,\mathcal{S},k}\right)^* \left(\Xi^{E,j,k} G^{E,\mathcal{S},k}\right) + \alpha_1^H \left(\Xi^{H,j,k} G^{H,\mathcal{S},k}\right)^* \left(\Xi^{H,j,k} G^{H,\mathcal{S},k}\right) \\ + \alpha_2 R^{(n),*} R^{(n)}\Big] \mathbf{w}^{(n),j,k} &= \\ \alpha_1^E \left(\Xi^{E,j,k} G^{E,\mathcal{S},k}\right)^* \Xi^{E,j,k} \mathbf{f}^{E,j,k} + \alpha_1^H \left(\Xi^{H,j,k} G^{H,\mathcal{S},k}\right)^* \Xi^{H,j,k} \mathbf{f}^{H,j,k} \\ + \alpha_2 R^{(n),*} \boldsymbol{\chi}^{(n-1)} \mathbf{e}^{\mathrm{inc},j,k}, \qquad (25)\end{aligned}$$

where $R^{(n)} = I - \boldsymbol{\chi}^{(n-1)} G^{E,\mathcal{D},k}$ and the superscript $*$ denotes the Hilbert adjoint operator.

The minimization with respect to the elements in $\boldsymbol{\chi}$ may be carried out explicitly, and we find

$$\left[\sum_{k=1}^{N_\mathrm{f}} \sum_{j=1}^{N_\mathrm{s}} \left|e_x^{(n),j,k}\right|^2 + \left|e_y^{(n),j,k}\right|^2\right] \chi_h^{(n)} = \sum_{k=1}^{N_\mathrm{f}} \sum_{j=1}^{N_\mathrm{s}} \overline{e_x^{(n),j,k}} w_x^{(n),j,k} + \overline{e_y^{(n),j,k}} w_y^{(n),j,k}, \qquad (26)$$

$$\left[\sum_{k=1}^{N_\mathrm{f}} \sum_{j=1}^{N_\mathrm{s}} \left|e_z^{(n),j,k}\right|^2\right] \chi_v^{(n)} = \sum_{k=1}^{N_\mathrm{f}} \sum_{j=1}^{N_\mathrm{s}} \overline{e_z^{(n),j,k}} w_z^{(n),j,k}, \qquad (27)$$

where $e_x^{(n),j,k}$ is the x-component of the vector $\mathbf{e}^{\mathrm{inc},j,k} + G^{E,\mathcal{D},k} \mathbf{w}^{(n),j,k}$, and the overline denotes the complex conjugate.

We note that the constant α_2 needs to be updated in each iteration. In these calculations we have for simplicity in iteration n let

$$\alpha_2^{(n)^{-1}} = \sum_{k=1}^{N_\mathrm{f}} \sum_{j=1}^{N_\mathrm{s}} \left\|\boldsymbol{\chi}^{(n-1)} \mathbf{e}^{\mathrm{inc},j,k}\right\|_{\mathcal{D}}^2, \qquad (28)$$

such that it is a constant in each iteration.

The electromagnetic inverse problem of finding anomalous currents is known to be a highly non-unique problem (Zhdanov, 2002; Abubakar et al., 2004). Due to this we introduce a regularizing term linearly into the cost functional to be able to incorporate prior information on the contrast. We now assume that $\mathcal{D}$ is discretized into N_p cells, arrange $\boldsymbol{\chi}$ into a vector of size $3 \times N_p$, $\boldsymbol{\chi} = (\chi_h, \chi_h, \chi_v)^T$, and introduce a new optimization problem as

$$\underset{\mathcal{W},\boldsymbol{\chi}}{\operatorname{argmin}} \quad \left(F_1\left(\mathcal{W},\boldsymbol{\chi}\right) + \lambda^2 F_2\left(\boldsymbol{\chi}\right)\right) = \underset{\mathcal{W},\boldsymbol{\chi}}{\operatorname{argmin}} \quad \left(F_1\left(\mathcal{W},\boldsymbol{\chi}\right) + \lambda^2 \left\|\boldsymbol{\Omega}\left(\boldsymbol{\chi} - \boldsymbol{\chi}^{\mathrm{ref}}\right)\right\|_{\mathcal{D}}^2\right). \tag{29}$$

Here F_2 is introduced to be able to incorporate prior information concerning the model. Further, $\boldsymbol{\chi}^{\mathrm{ref}}$ is some reference model, e.g. expected solution, $\boldsymbol{\Omega}$ is some weighting matrix and $\lambda \in \mathbb{R}$ a weighting parameter controlling the tradeoff between $F_1\left(\mathcal{W},\boldsymbol{\chi}\right)$ and $F_2\left(\boldsymbol{\chi}\right)$ which needs to be chosen appropriately not to emphasize only one of the terms.

The weights $\boldsymbol{\Omega}$ are given by the matrix

$$\boldsymbol{\Omega} = \begin{pmatrix} \boldsymbol{\Omega}_{11} & \boldsymbol{\Omega}_{12} & \boldsymbol{\Omega}_{13} \\ \boldsymbol{\Omega}_{21} & \boldsymbol{\Omega}_{22} & \boldsymbol{\Omega}_{23} \\ \boldsymbol{\Omega}_{31} & \boldsymbol{\Omega}_{32} & \boldsymbol{\Omega}_{33} \end{pmatrix}, \tag{30}$$

where $\boldsymbol{\Omega}_{ij}$ are $N_p \times N_p$ sub-matrices. They can be chosen to introduce different effects, e.g.

- Freeze parts of the model by choosing the diagonal elements of $\boldsymbol{\Omega}_{ii}$ large and $\boldsymbol{\Omega}$ elsewise zero, thus keeping the reconstruction close to the reference model.

- Introduce spatial correlations between cells by choosing off-diagonal cells non-zero in some of the sub-matrices.
- Introduce structural information, allowing for sharp boundaries where interfaces are believed to occur, by applying smoothing filters only to gridcells away from the interface.
- Introduce correlations between χ_h and χ_v by choosing $\mathbf{\Omega}_{13}, \mathbf{\Omega}_{23}, \mathbf{\Omega}_{31}, \mathbf{\Omega}_{32}$ nonzero.

In our examples $\mathbf{\Omega}$ is chosen to be second order smoothing filters in the horizontal and vertical directions acting on χ_h and χ_v individually, thus introducing spatial correlations between neighboring cells. Further, the reference model is $\boldsymbol{\chi}^{\text{ref}} = 0$ to emphasize only the smoothness of the solution. Different weights are not put on horizontal and vertical smoothing as the purpose here is numerical stabilization. The parameter λ is chosen by observation such that the term F_2 does not dominate the cost functional, and it is relaxed towards zero as the iterations proceed to not over emphasize the prior-term. Other strategies for choosing λ are mentioned in the discussion.

We note that this second term does not affect the estimation of $\mathbf{w}^{j,k}$. However, the estimators for χ_h and χ_v are changed, and due to the spatial correlations equations 26 and 27 no longer hold point wise. Thus, in each iteration we must solve a linear system of equations specified by the correlations determined by $\mathbf{\Omega}$ to estimate the contrast.

This problem is sensitive to a number of factors due to the ill-posedness; the minimization method itself, inital model, choice of stabilizer and the number of iterations in the contrast source and contrast update. Although the alternating scheme leads to a well defined minimization problem for the contrast, the problem of finding the contrast sources is non-unique, and in the presence of noise the solution for the contrast may become unstable. The choice of minimization method is taken from van den Berg and Kleinman (1997). This has been explored in several articles, see for instance Abubakar and van den Berg (2002); Abubakar et al. (2004); Abubakar and van den Berg (2004), and has proven quite stable. A different alternating algorithm based on the integral equation framework has been presented in Cox and Zhdanov (2008) for airborne EM inversion. The choice of stabilizer is a classical choice, recently applied to anisotropic CSEM inversion by Newman et al. (2010), and is well explored in the geophysical setting. Choosing an initial model in actual mCSEM prospecting is a careful and long exercise based on geophysical data from several sources, especially in complex areas. We have therefore not made any discussion on how to choose initial models. For the first synthetic example, two different initial models are tested to say something about the stability of the method. In the second synthetic example we consider only one initial model to demonstrate how the TIV extension may be necessary, while for the real data examples the initial models are based on seismic sections.

RESULTS

In this section we present both synthetic and real data examples using the CSI method on mCSEM data. In the synthetic examples random noise is added according to

$$\tilde{\mathbf{f}}^{E,j,k} = \mathbf{f}^{E,j,k} + p\frac{\max_j \left|\mathbf{f}^{E,j,k}\right|}{\sqrt{2}}\left(\xi^{E,j,k} + \mathrm{i}\eta^{E,j,k}\right), \tag{31}$$

$$\tilde{\mathbf{f}}^{H,j,k} = \mathbf{f}^{H,j,k} + p\frac{\max_j \left|\mathbf{f}^{H,j,k}\right|}{\sqrt{2}}\left(\xi^{H,j,k} + \mathrm{i}\eta^{H,j,k}\right), \tag{32}$$

where p is a percentage and $\xi^{E,j,k}, \xi^{H,j,k}, \eta^{E,j,k}, \eta^{H,j,k}$ are 3×1 vectors where the components are normal distributed random numbers with 0 mean and standard deviation 0.25. 95% of the samples from this distribution will lie within the interval $[-0.5, 0.5]$. The regularization parameter is chosen in a similar manner as described in Newman et al. (2010). Further, when comparing the results to the known solution the error is measured in each pixel as

$$\epsilon_{h/v} = \frac{\left|\sigma_{h,v} - \sigma_{0,h/v}\right|}{\sigma_{0,h/v}}, \tag{33}$$

that is, the relative difference in conductivity.

Slab example

To investigate the stability of the implemented CSI method, we consider the model shown in Figure 2. Figures 2, 3, 4 and 5 show the cross section beneath the line of receivers at $y = 0$m, while Figure 6 shows the cross line plane $x = 0$m to demonstrate how the method performs in the cross line direction. The anomaly stretches 1000m both into and out of the plane. Single frequency data at 0.25Hz for inline electric and crossline magnetic field components are inverted using two different initial models, shown in Figure 3. Figure 3(a) display a relatively good initial model, the anomaly placed within the actual anomaly and with the correct conductivity of 0.01S/m, while Figure 3(b) displays a bad initial model which do not comply in neither position, nor conductivity, with the true anomaly. The initial anomalies stretches across all of $\mathcal{D}$ in the y-direction. 8% noise is added to the data. The domain $\mathcal{D}$ is described by $-7000\text{m} \leq x \leq 7000\text{m}$, $-2000\text{m} \leq y \leq 2000\text{m}$, $1100\text{m} \leq z \leq 1900\text{m}$ with meshsize $\Delta x = 250\text{m}, \Delta y = 500\text{m}, \Delta z = 50\text{m}$. We choose to compare only the vertical conductivity with the true model, which is isotropic, since this configuration is sensitive only to the vertical conductivity of the resistor (Løseth and Ursin, 2007; Newman et al., 2010). Each iteration of the algorithm used on average about 405 seconds on a single 2.83GHz Intel Xeon CPU, needing in total approximately 450MB memory.

Figures 4(a) and 4(b) show that the method is able to determine the inline lateral extent quite accurately in both cases, but the depth position seems to depend more on the initial model. Further, Figure 6 shows that the cross line extent is not accurately reconstructed. Figures 5(a) and 5(b) show the difference between the real and reconstructed domain $\mathcal{D}$ as defined in equation 33. It is clear that the conductivity estimates are not as low as the true conductivity, which is reasonable due to the smoothing regularizer which makes the estimated anomaly both ticker and wider. These figures also clearly show that a better estimate is obtained using a good initial model. Figure 7 shows the convergence history for the two cases, and we observe that with a good initial model convergence is reached in fewer iterations. At this point the datafit is approximately the same, but for the good initial model the prior term is larger when the iterations are terminated. The datafit when using the bad initial model is shown in Figure 8.

Anisotropic overburden

To demonstrate the anisotropic inversion we consider a model with an anisotropic overburden as shown in Figure 9. The anisotropic layer is of infinite horizontal extent with $\sigma_h = 2\text{S/m}$ and $\sigma_v = 0.5\text{S/m}$. The reservoir stretches 2000m into and out of the plane with invariant cross section in the xz-plane. The conductivity in the reservoir is 0.01S/m. Again, single frequency data at 0.25Hz for inline electric and crossline magnetic field components are inverted, using both an isotropic and TIV inversion. 8% noise is added to the data. The domain $\mathcal{D}$ is described by $-15000\text{m} \leq x \leq 15000\text{m}$, $-4000\text{m} \leq y \leq 4000\text{m}$, $800\text{m} \leq z \leq 2000\text{m}$ with meshsize $\Delta x = 500\text{m}, \Delta y = 500\text{m}, \Delta z = 50\text{m}$. Each iteration of the algorithm used on average about 1500 seconds on a single 2.83GHz Intel Xeon CPU, needing in total approximately 1.4GB memory. The initial model is taken to be isotropic as in Figure 10.

Figure 11 shows the isotropic result. It is not able to place the reservoir beneath the anisotropic layer, and predicts only a more resistive section in the overburden. The TIV inversion, however, is able to introduce anisotropy in the overburden and place an anomaly beneath this layer, as shown in Figure 12. Although the anisotropic layer is not accurately reconstructed and the conductivity estimate in the reservoir is too high the result clearly indicates the presence of anisotropy in the overburden and the presence of a resistive anomaly.

Troll 2003

We now demonstrate the method on two datasets from the Troll field in the Norwegian North Sea. Since both surveys were collected along lines the results are displayed as cross-sections along the source/receiver line.

The first dataset was collected by Statoil over the Troll West Gas Province (TWGP) in 2003, and the setting is described in Johansen et al. (2005). The source was a dipole of 230m length and a peak current of approximately 1000A. The fundamental frequency was 0.25Hz, and although several harmonics were recorded only the fundamental frequency is used in this inversion, as using higher frequencies did not make large differences in the image of TWGP. 24 receivers were dropped on the seabed, all of which measured the inline electric field. A subset of the receivers also measured the crossline magnetic field.

The background model consists of a sea layer, with depth equal to the arithmetic mean of the receiver depths and conductivity 3.3S/m, and a homogeneous halfspace with conductivity 0.35S/m. The halfspace conductivity was chosen by modeling comparison with the real data. Upon inspecting the seismic section the domain $\mathcal{D}$ was chosen as $-6000\text{m} \leq x \leq 7750\text{m}$, $-1000\text{m} \leq y \leq 1000\text{m}$ and $1000\text{m} \leq z \leq 2000\text{m}$

with grid size $\Delta x = 250\text{m}, \Delta y = 250\text{m}, \Delta z = 50\text{m}$. The initial model was chosen as shown in Figure 13, which is seen to be shorter and more shallow than the reservoir.

The result from the isotropic inversion is displayed in Figure 14 laid over a seismic section. We observe that the anomaly is moved slightly deeper and extended laterally compared to the initial model, and that it corresponds well with the seismic image. For this case we also present the results when the domain $\mathcal{D}$ is extended 2km in each direction laterally and 500m in each direction vertically compared to the domain described above. This is shown in Figure 15. We see that the results are very similar, which might indicate that the background model is well chosen.

The results from the TIV inversion are displayed in Figure 16. We observe that also the TIV inversion move the anomaly slightly deeper and extends it laterally to approximately the same position as the isotropic inversion. From Figure 16(a) and Figure 16(b) we observe that almost no contrast is estimated for σ_h. This is as expected since the signal propagation in the reservoir is governed by the vertical conductivity σ_v (Løseth, 2007), and thus when we apply a smoothing filter the profile for σ_h will be smoothed towards zero. The contrast estimated for the vertical conductivity is larger than that estimated in the isotropic case.

This data set has been treated in several articles earlier, see e.g. Plessix and Mulder (2008); Abubakar et al. (2009). Comparing to the results obtained by Abubakar et al. (2009) we observe that the lateral extent of the anomaly in the inline direction is similar, but our result is slightly deeper. The crossline extent estimated by Abubakar et al. (2009) is wider than our chosen domain $\mathcal{D}$, and will cause differences in our results. However, since we only have line data this extent cannot be expected to be accurate. We note that their inversion was performed using data at both 0.25Hz and 0.75Hz, but only using inline electric field data. This differs from us. Our results predict a slightly higher resistivity contrast, which may be due to the differences mentioned. Turning to the results shown by Plessix and Mulder (2008) the inline extent of the anomaly is similar to ours, and their depth also seems to be approximately that shown by our results. Again, our resistivity estimate is higher, but again the inversion results obtained by Plessix and Mulder (2008) is based on inline electric field data for three frequencies, 0.25Hz, 0.75Hz and 1.25Hz.

Troll 2008

The second dataset was collected over the Troll field in 2008 at a slightly different location than the example above. The survey was at the same location and similar to the survey described in Farrelly et al. (2004); Johnstad et al. (2005). This line now crosses three laterally separated anomalies as shown in Figure 2 in Farrelly et al. (2004), the largest being the TWGP, but also the Troll West Oil Province (TWOP) further west which lies slightly deeper and has less contrast. The inversion was now carried out on the fundamental frequency and it's first odd harmonic, i.e. 0.25Hz and 0.75Hz, as the fundamental frequency alone was not able to pick up the smaller anomalies. Further, the smaller anomalies only appeared after a sufficient level of data misfit was achieved. All receivers measured the inline electric and crossline magnetic fields.

The background model again consists of a sea layer, with depth equal to the arithmetic mean of the receiver depths and conductivity 3.3S/m, and a homogeneous halfspace with conductivity 0.35S/m. Upon inspecting the seismic section the domain $\mathcal{D}$ was chosen as $-10000\text{m} \leq x \leq 12000\text{m}$, $-1000\text{m} \leq y \leq 1000\text{m}$ and $1000\text{m} \leq z \leq 2000\text{m}$ with grid size $\Delta x = 250\text{m}, \Delta y = 250\text{m}, \Delta z = 50\text{m}$. The initial model was chosen as a rectangular, resistive body placed between $7000\text{m} \leq x \leq 8750\text{m}$, $1550\text{m} \leq z \leq 1600\text{m}$ as shown in Figure 17. A small anomaly is expected approximately at this position as shown in Figure 2 in Farrelly et al. (2004).

The results are displayed in Figures 18 and 19, which show the isotropic and TIV inversion results, respectively. Figures 20(a) and 20(b) show slices through the reconstructed domain $\mathcal{D}$ for the TIV inversion. The same effect as in the previous example concerning the estimate for σ_h is observed in Figure 19(a). Figure 18 shows that the initial box only remains with a weak contrast, while the large anomaly connected to TWGP is introduced. However, Figure 19(b) displays a brighter anomaly in σ_v at the approximate position of the initial model, the large anomaly from TWGP is introduced, and even a small anomaly to the left of TWGP, approximately at the position of the TWOP. The large anomaly from the TIV inversion is however more spread out than the isotropic estimate.

We again observe the nice fit with the seismic. However, the small anomaly close to TWOP in Figure 19(b) is slightly too close to TWGP. This might be an effect due to the bias introduced by the smoothing regularization, but could also lead to questioning this anomaly. The slightly red color in Figure 19(a) might indicate that the background model is not optimal, and illustrates the difficulty of choosing an appropriate background model. This will be further mentioned in the discussion.

The additional degrees of freedom introduced by allowing a TIV in stead of isotropic medium naturally results in a better data fit. The term in the cost functional corresponding to fit in $\mathbf{e}$ decrease from 0.0384 to 0.0341, and the term corresponding to $\mathbf{h}$ from 0.0234 to 0.0226. This may also be a part of the explanation for why the smaller anomalies appear in the TIV inversion, but not in the isotropic. The convergence histories for this data set are shown in Figure 21.

DISCUSSION

Although we have found the CSI method to be applicable to real field data we may point at several critical points with this method that may lead to difficulties in the inversion. The most critical point is choosing an appropriate background model, which in turn means having a good perception of the over- and underburden. If it is not appropriately chosen the algorithm will attempt to explain these effects within the domain $\mathcal{D}$, and may thus lead to an incorrect inversion. This is especially important if the anomalies are small or have weak contrasts. The theory presented is not limited to a planarly layered background, as is chosen in the examples. However, with this choice the Green's tensors and incident fields may be calculated very rapidly, ensuring a fast algorithm under these limitations.

Ideally one would like to invert for the whole subsurface simultaneously, but this will normally give a variety of resulting models with different background resitivities in combination with different structures of anomalies, depending on different prior data interpretations. Thus, one finally has to select the most probable models based on seismics and possibly well logs. CSI is a suitable tool for investigating if the mCSEM data contain responses from an anomaly for a suite of probable background models, and may thus be helpful in this final selection.

Compared to methods which discretize the entire subsurface using e.g. finite differences (Newman et al., 2010), the major advantage of integral equation type methods is the opportunity to consider only a very limited volume within a chosen background, which allows for an algorithm with low memory requirements in appropriate situations. However, the efficiency relies on evaluating the integral operators fast, which is significantly faster in for instance plane layered backgrounds compared to a general background. The anomalous domain can be chosen to cover the entire subsurface, but the advantage of using integral equations may then be lost compared to finite difference and finie element methods. Compared to other integral equation methods the biggest difference lies in the approximation of a non-linear problem by two linear problems, although a similar idea is considered in Cox and Zhdanov (2008). For instance, Zhdanov and Hursan (2000) consider integral equation inversion, but the third term in equation 21 is not considered in their cost functional and does thus not facilitate the splitting used in the CSI method.

When introducing prior information on the model several issues needs to be addressed. Obviously an appropriate weighting matrix Ω needs to be chosen. In our examples we used this term only for numerical stabilization, and thus chose equal weights on horizontal and vertical smoothing and λ such that the prior term did not dominate the cost functional. However, it may be argued that different weights should be put on horizontal and vertical smoothing due to layering in the earth. Further, if the prior information should be appropriately emphasized λ needs to be carefully chosen, and several strategies have been investigated for this. A particular choice is to use the L-curve criterion (Hansen and O'leary, 1993), which involves solving the inverse problem for several different λ and is thus very time consuming for large-scale geophysical inverse problems. A fast approach to approximating this value was developed by Rabben and Ursin (2007), cast in a Bayesian setting. Zhdanov (2002) suggests choosing the regularization parameter according to an estimated noise level in the weighted data, and also cross validation techniques have been studied, see e.g. Tenorio (2001) for a review and the references therein. Another strategy has been explored in conjunction with Occam's inversion (Constable et al., 1987). It is also possible to regularize the problem using a multiplicative regularizer, thus avoiding having to choose this parameter altogether (Abubakar and van den Berg, 2004). Although our strategy for choosing this parameter is not optimal in any sense, it is often performed due to it being less time consuming than the procedures mentioned above.

Finally, we wish to emphasize the importance of analyzing the data and prior information before performing an inversion. Determining which parameters can be imaged and being aware of the bias introduced through the chosen regularization is important, and should be taken into account also when analyzing the output from inversion algorithms. Several inversions using different regularizations and different parameters should be performed to study the consistency of the results to assess the associated uncertainties.

CONCLUSIONS

We have demonstrated a CSI inversion method for mCSEM experiments in TIV anisotropic media. The method is tested on two real field examples, both from the Troll field offshore Norway.

The method is based on an integral equation framework, thus relying on choosing an appropriate background model. It is formulated as an optimization problem minimizing a cost functional which enforces both data fidelity and that the solution fits with the electromagnetic equivalent of the Lippmann-Schwinger equation for the scalar Helmholtz equation. The latter term may be viewed as a natural regularizer.

A method for introducing prior information on the model is also introduced linearly into the cost functional. This may be used for e.g. numerical stabilization, structural information, keeping the solution close to an expected solution or correlating the horizontal and vertical conductivities. This regularization relies on choosing a regularization parameter, for which several strategies are discussed.

We found that the method is applicable to real field data, and the examples demonstrate that TIV inversion is preferred over the isotropic in some situations to properly image the subsurface. However, information concerning the background model is needed for a successful result. The method should thus be viewed in context with other methods which discretize the entire survey area.

ACKNOWLEDGEMENTS

The authors wish to thank the Troll license for permission to publish this work. Torgeir Wiik acknowledges Statoil ASA for sponsoring his Ph.D. project. Bjørn Ursin has received financial support from VISTA and from the Norwegian Research Council through the ROSE project. We greatly appreciate the contructive comments and critisism received from Assosciate Edior Evert Slob, as well as those from Alexander Gribenko, Aria Abubakar and one anonymous reviewer.

REFERENCES

Abubakar, A., T. M. Habashy, V. L. Druskin, L. Knizhnerman, and D. Alumbaugh, 2008a, 2.5D forward and inverse modeling for interpreting low-frequency electromagnetic measurements: Geophysics, **73**, F165–F177.

Abubakar, A., T. M. Habashy, M. Li, and J. Liu, 2009, Inversion algorithms for large-scale geophysical electromangetic measurement: Inverse Problems, **25**, 30pp.

Abubakar, A., W. Hu, P. M. van den Berg, and T. M. Habashy, 2008b, A finite-difference contrast source inversion method: Inverse Problems, **24**, 17pp.

Abubakar, A., and P. M. van den Berg, 1998, Three-dimensional nonlinear inversion in cross-well electrode logging: Radio Science, **33**, 989–1004.

———, 2000, Three-dimensional inverse scattering applied to cross-well induction sensors: IEEE Transactions on Geoscience and Remote Sensing, **38**, 1669–1681.

———, 2002, The Contrast Source Inversion method for location and shape reconstructions: Inverse Problems, **18**, 495–510.

———, 2004, Iterative forward and inverse algorithms based on domain integral equations for three-dimensional electric and magnetic objects: Journal of Computational Physics, **195**, 236–262.

Abubakar, A., P. M. van den Berg, and J. J. Mallorqui, 2002, Imaging of biomedical data using a multiplicative regularized Contrast Source Inversion method: IEEE Transactions on Microwave Theory and Techniques, **50**, 1761–1771.

Abubakar, A., P. M. van den Berg, and S. Y. Semenov, 2004, A robust interative method for Born inversion: IEEE Transactions on Geoscience and Remote Sensing,

42, 342–354.

Colton, D., and R. Kress, 1992, Inverse acoustic and electromagnetic inverse scattering theory: Springer Verlag.

Constable, S. C., R. L. Parker, and C. G. Constable, 1987, Occam's inversion: A practical algorithm for generating smooth models from electromagnetic sounding data: Geophysics, **52**, 289–300.

Cox, L. H., and M. S. Zhdanov, 2008, Advanced computational methods of rapid and rigorous 3-d inversion of airborne electromagnetic data: Communications in Computational Physics, **3**, 160–179.

de Hoop, A. T., 1995, Handbook of radiation and scattering of waves: Academic Press.

Eidesmo, T., S. Ellingsrud, L. M. MacGregor, S. Constable, M. C. Sinha, S. Johansen, F. N. Kong, and H. Westerdal, 2002, Sea Bed Logging (SBL), a new method for remote and direct idetification of hydrocarbon filled layers in deepwater areas: First Break, **20**, 144–152.

Farrelly, B., C. Ringstad, S. E. Johnstad, and S. Ellingsrud, 2004, Remote characterization of hyrdocarbon filled reservoirs at the Troll field by sea bed logging: EAGE Fall Research Workshop on Advances in Seismic Acquisition Technology.

Feng, H., V. Galdi, and D. A. Castañon, 2003, An object-based contrast source inversion method for homogeneous targets: Subsurface sensing technologies and applications, **4**, 355–374.

Green, G., 1828, An essay on the application of mathematical analysis to the theories of electricity and magnetism: T. Wheelhouse, Nottingham.

Hansen, P. C., and D. P. O'leary, 1993, The use of the L-curve in the regularization of discrete ill-posed problems: SIAM Journal on Scientific Computing, **14**, 1487–1503.

Johansen, S. E., H. E. F. Amundsen, T. Røsten, S. Ellingsrud, T. Eidesmo, and A. H. Bhuyian, 2005, Subsurface hydrocarbons detected by electromagnetic sounding: First Break, **23**, 31–36.

Johnstad, S. E., B. A. Farrely, and C. Ringstad, 2005, Em seabed logging on the troll field: EAGE 67th Conference & Exhibition - Madrid, Spain.

Kong, F. N., S. E. Johnstad, T. Røsten, and H. Westerdal, 2008, A 2.5D finite-element-modeling difference method for marine csem modeling in stratified anisotropic media: Geophysics, **73**, F9–F19.

Løseth, L. O., 2007, Modelling of controlled source electromagnetic data: PhD thesis, Norwegian University of Science and technology.

Løseth, L. O., and B. Ursin, 2007, Electromagnetic fields in planarly layered anisotropic media: Geophysical Journal International, **170**, 44–80.

McOwen, ., 1996, Partial differential equations. methods and applications: Prentice-Hall.

Newman, G., 1995, Crosswell electromagnetic inversion using integral and differential equations: Geophysics, **60**, 899–911.

Newman, G. A., M. Commer, and J. J. Carazzone, 2010, Imaging csem data in the presence of electrical anisotropy: Geophysics, **75**, F51–F61.

Newman, G. A., and G. M. Hoversten, 2000, Solution strategies for two and three-dimensional electromagnetic inverse problems: Inverse Problems, **16**, 1357–1375.

Plessix, R.-E., and W. A. Mulder, 2008, Resistivity imaging with controlled-source electromagnetic data: depth and data weighting: Inverse Problems, **24**, 22pp.

Rabben, T. E., and B. Ursin, 2007, Nonlinear least squares inversion of reflection coefficients using bayesian regularization: Presented at the Proceedings of the SEG Annual Meeting 2007.

Stratton, J. A., 1941, Electromagnetic theory: McGraw-Hill.

Tenorio, L., 2001, Statistical regularization of inverse problems: SIAM Review, **43**, 347–366.

Tikhonov, A. N., and V. Y. Arsenin, 1977, Solution of ill-posed problems: W.H.Winston and Sons.

Ursin, B., 1983, Review of elastic and electromagnetic wave propagation in horizontally layered media: Geophysics, **48**, 1063–1081.

van den Berg, P. M., 1984, Iterative computational techniques in scattering based upon the integrated square error criterion: IEEE Transactions on Antennas and Propagation, **32**, 1063–1071.

van den Berg, P. M., and R. Kleinman, 1997, A contrast source inversion method: Inverse Problems, **13**, 1607–1620.

Wannamaker, P. E., G. W. Hohmann, and W. A. SanFilipo, 1984, Electromagnetic modelling of three-dimensional bodies in layered earths using integral equations: Geophysics, **49**, 60–74.

Ward, S. H., and G. W. Hohmann, 1987, Electromagnetic theory for geophysical applications, *in* Electromagnetic methods in applied geophysics: Society of Exploration Geophysicists, 131–311.

Zhdanov, M., and G. Hursan, 2000, 3d electromagnetic inversion based on quasianalytical approximation: Inverse Problems, **16**, 1297–1322.

Zhdanov, M. S., 2002, Geophysical inverse theory and regularization problems: Elsevier.

Figure 1: Schematic intersection of the model.

Figure 2: Model of slab example.

Figure 3: Initial models for the two inversions on the slab model. (a) Good initial model, (b) Bad initial model.

Figure 4: Inversion results for σ_v on the slab model. (a) Result from good initial model, (b) Result from bad initial model.

Figure 5: Error (ϵ) of inversion results in $\mathcal{D}$ on a logarithmic scale. (a) Error with good initial model, (b) Error with bad initial model.

Figure 6: Inversion result for σ_v with good initial model. Cross line profile at $x = 0$m.

Figure 7: The cost functional evolution for the for the slab model. (a) Cost functional from good initial model, (b) Cost functional from bad initial model.

Figure 8: Final datafit for scattered field from bad initial model. Top panel: e_x, bottom panel: h_y. (a) Magnitude, (b) Phase.

Figure 9: Real model in anisotropic example. (a) σ_h, (b) σ_v. Figure 10: Isotropic initial model for the anisotropic example. Figure 11: Isotropic result for anisotropic example. Figure 12: TIV result for anisotropic example. (a) σ_h, (b) σ_v. Figure 13: Initial model for the 2003 Troll dataset. Triangles denote receiver positions, red rectangle marks main reservoir.

Figure 14: Isotropic inversion result for the 2003 Troll dataset laid over a seismic section. Triangles denote lateral receiver positions, red rectangle marks main reservoir.

Figure 15: Isotropic results for the 2003 Troll dataset with different size on $\mathcal{D}$. Triangles denote lateral receiver positions. (a) Small $\mathcal{D}$, (b) Large $\mathcal{D}$.

Figure 16: TIV inversion results for the 2003 Troll dataset laid over a seismic section.

Triangles denote lateral receiver positions, red rectangle marks main reservoir. (a) σ_h, (b) σ_v.

Figure 17: Initial model for the 2008 Troll dataset laid over a seismic section. Triangles denote lateral receiver positions, red rectangles mark reservoirs.

Figure 18: Isotropic inversion result for the 2008 Troll dataset laid over a seismic section. Triangles denote lateral receiver positions, red rectangles mark reservoirs.

Figure 19: TIV inversion results for the 2008 Troll dataset laid over a seismic section. Triangles denote lateral receiver positions, red rectangles mark reservoirs. (a) σ_h, (b) σ_v.

Figure 20: Slices orthogonal to the sailing line through reconstructed domain $\mathcal{D}$ showing TIV inversion results for the 2008 Troll dataset. (a) σ_h, (b) σ_v.

Figure 21: Convergence history for the Troll 2008 example. (a) Isotropic, (b) TIV.

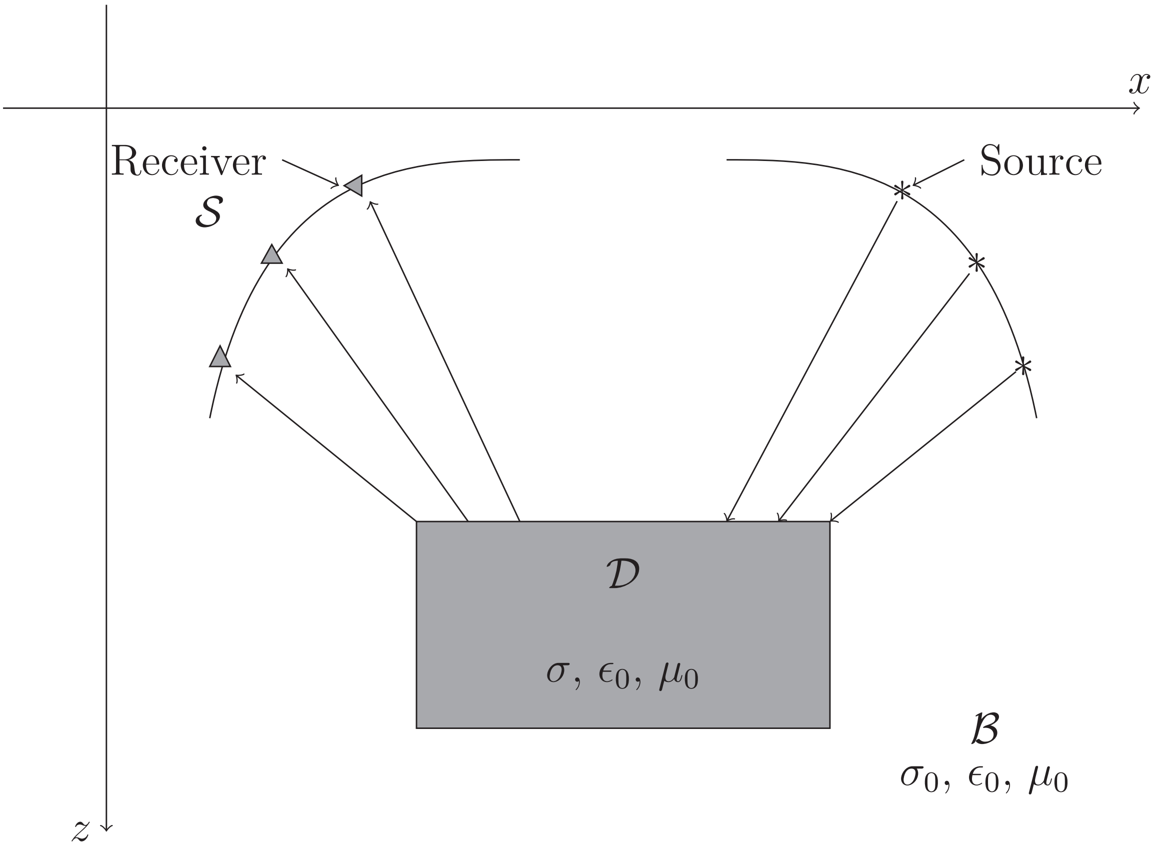

Figure 1: Schematic cross-section of the model.

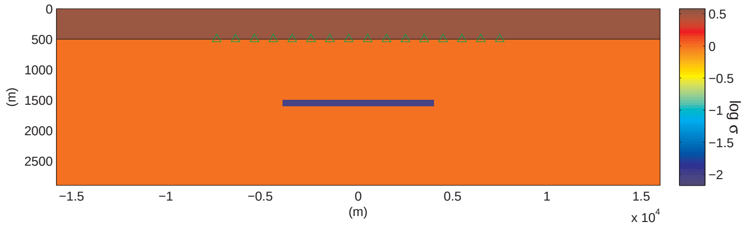

Figure 2: Model of slab example.

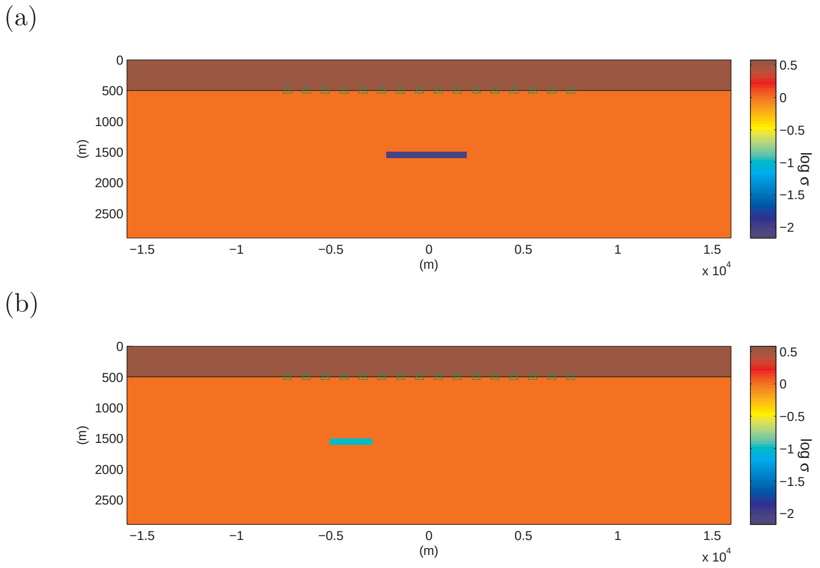

Figure 3: Initial models for the two inversions on the slab model. (a) Good initial model, (b) Bad initial model.

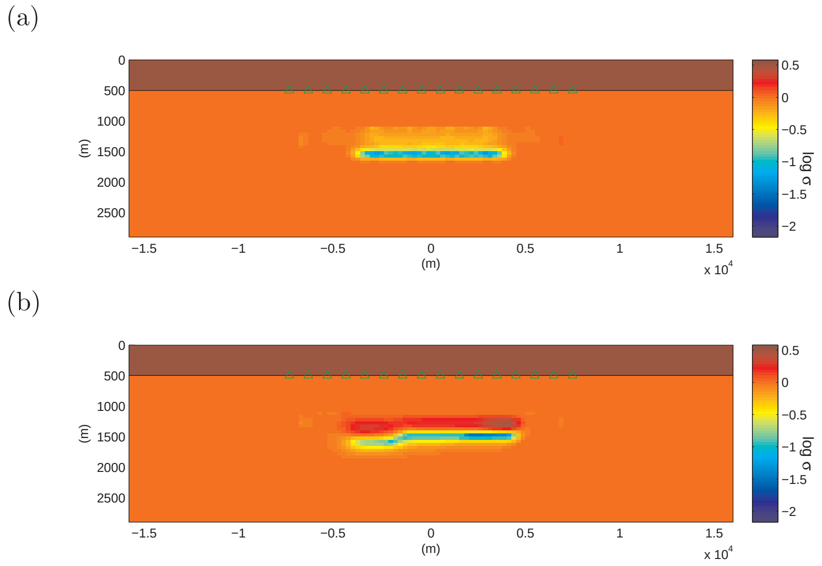

Figure 4: Inversion results for σ_v on the slab model. (a) Result from good initial model, (b) Result from bad initial model.

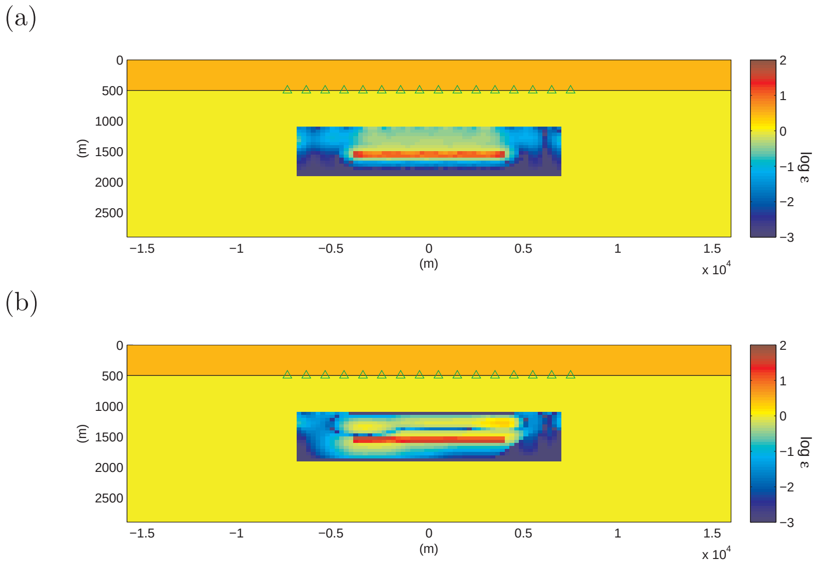

Figure 5: Error (ϵ) of inversion results in $\mathcal{D}$ on a logarithmic scale. (a) Error with good initial model, (b) Error with bad initial model.

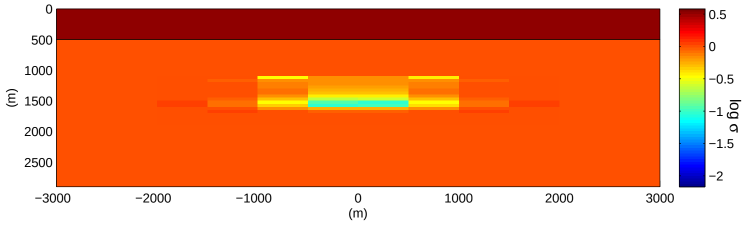

Figure 6: Inversion result for σ_v with good initial model. Cross line profile at $x = 0$m.

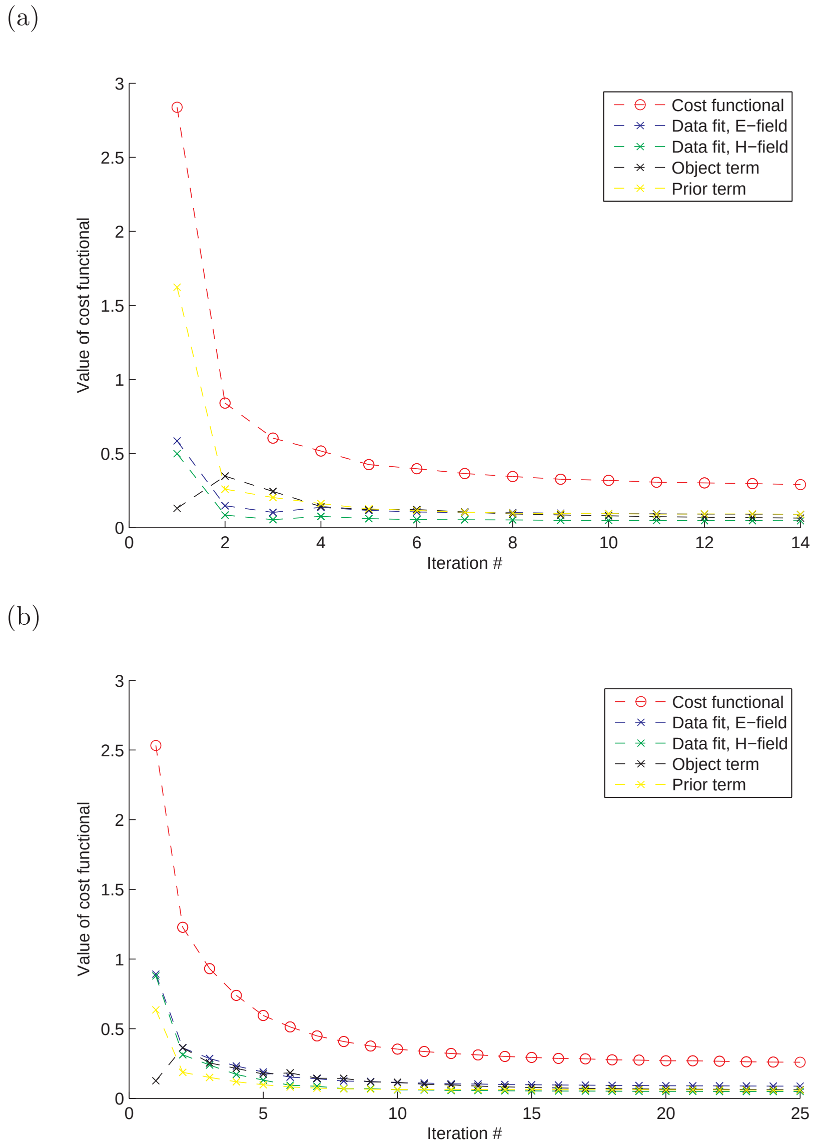

Figure 7: The cost functional evolution for the for the slab model. (a) Cost functional from good initial model, (b) Cost functional from bad initial model.

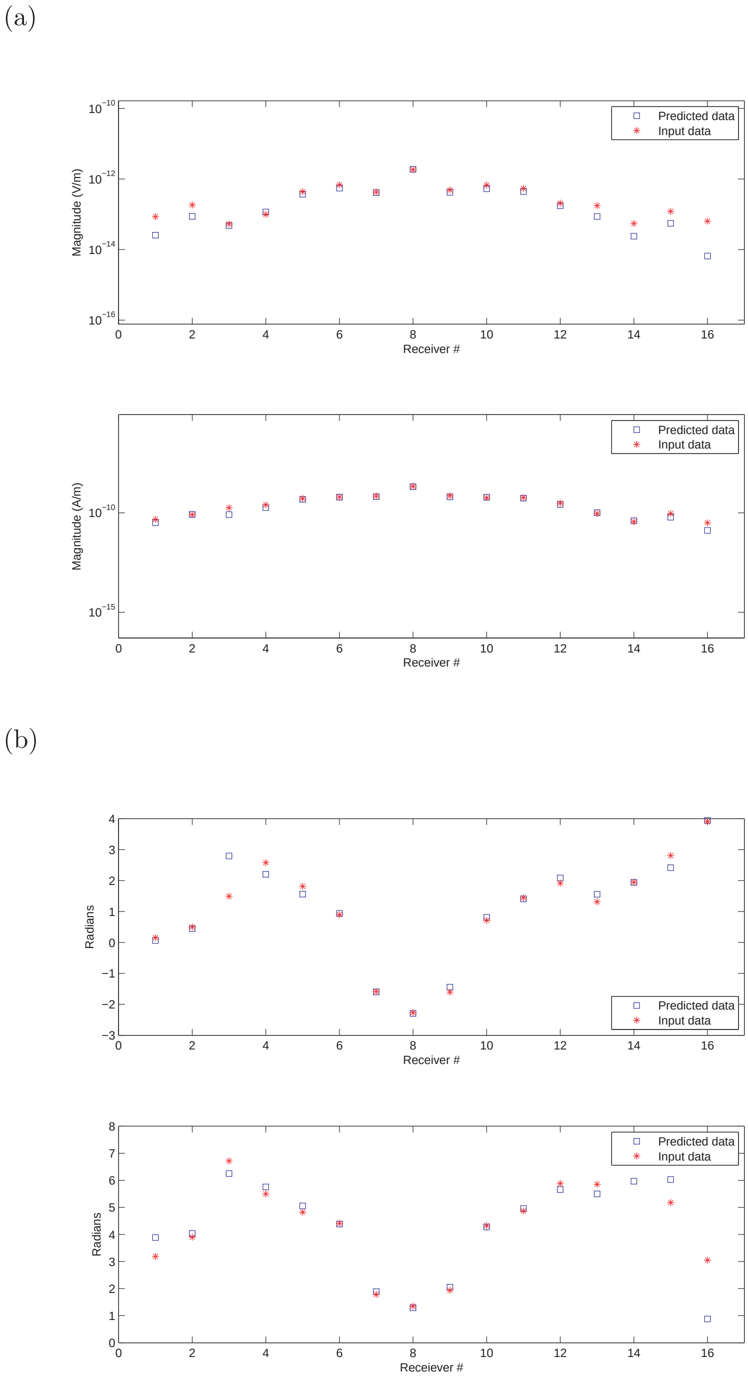

Figure 8: Final datafit for scattered field from bad initial model. Top panel: e_x, bottom panel: h_y. (a) Magnitude, (b) Phase.

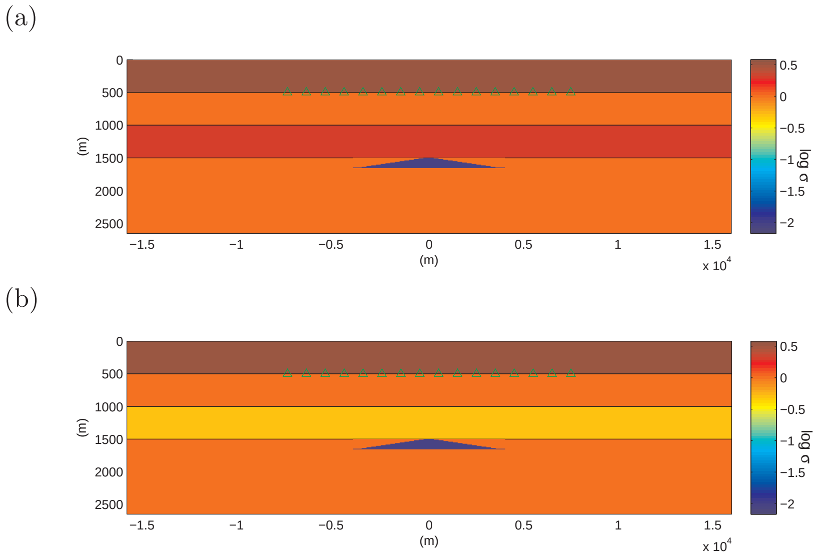

Figure 9: Real model in anisotropic example. (a) σ_h, (b) σ_v.

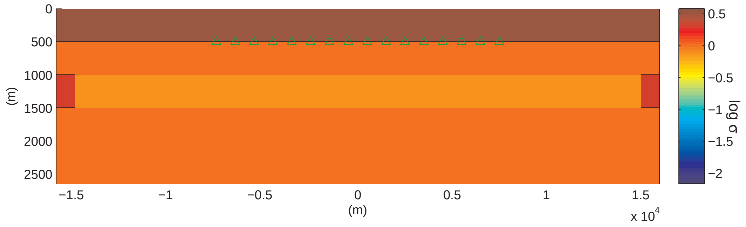

Figure 10: Isotropic initial model for the anisotropic example.

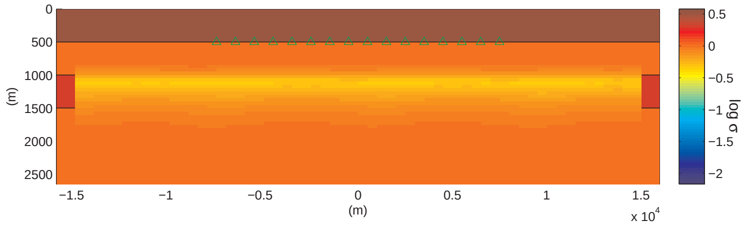

Figure 11: Isotropic result for anisotropic example.

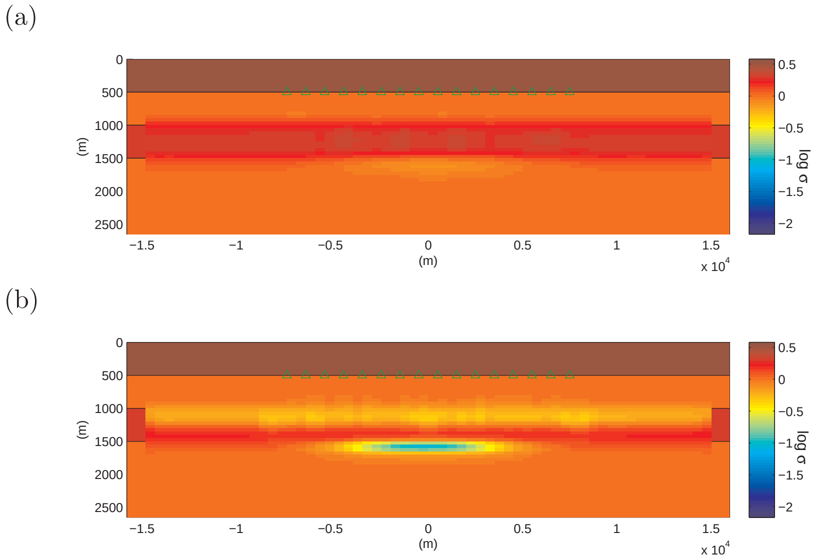

Figure 12: TIV result for anisotropic example. (a) σ_h, (b) σ_v.

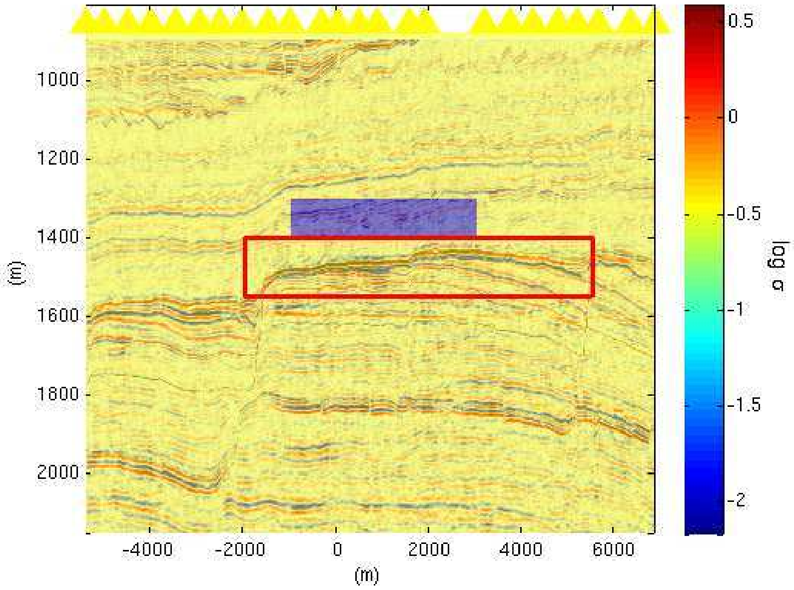

Figure 13: Initial model for the 2003 Troll dataset. Triangles denote receiver positions, red rectangle marks main reservoir.

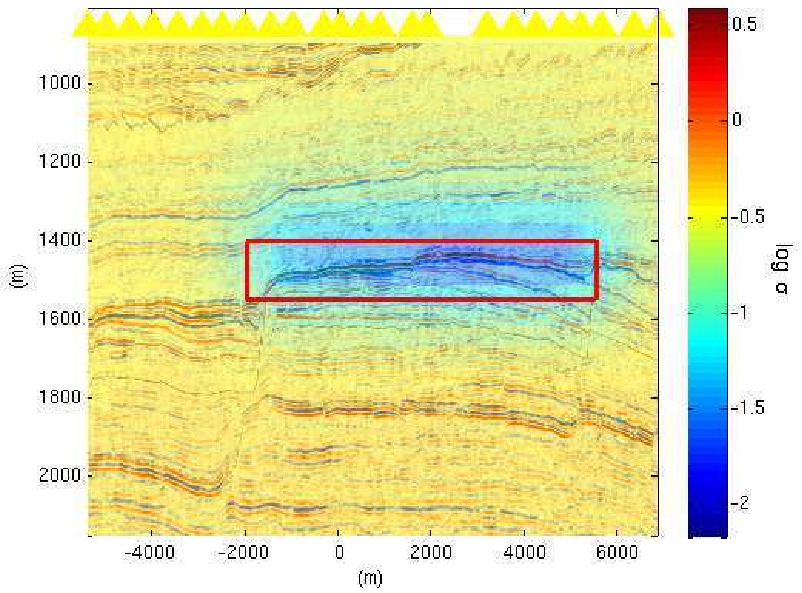

Figure 14: Isotropic inversion result for the 2003 Troll dataset laid over a seismic section. Triangles denote lateral receiver positions, red rectangle marks main reservoir.

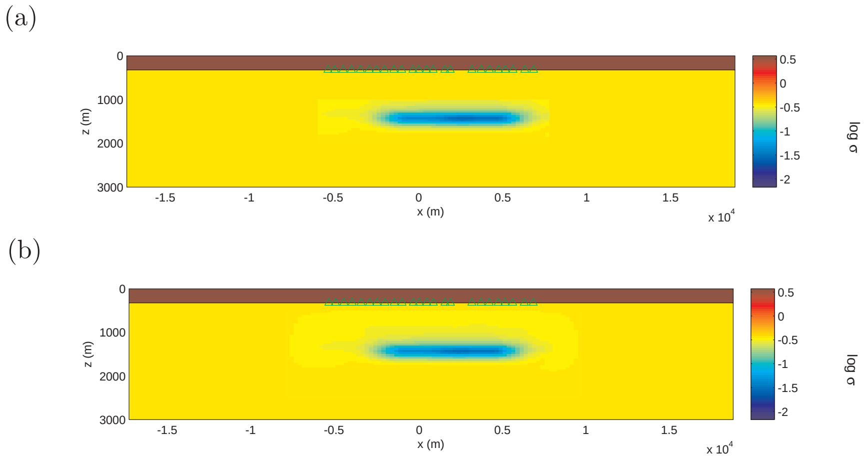

Figure 15: Isotropic results for the 2003 Troll dataset with different size on $\mathcal{D}$. Triangles denote lateral receiver positions. (a) Small $\mathcal{D}$, (b) Large $\mathcal{D}$.

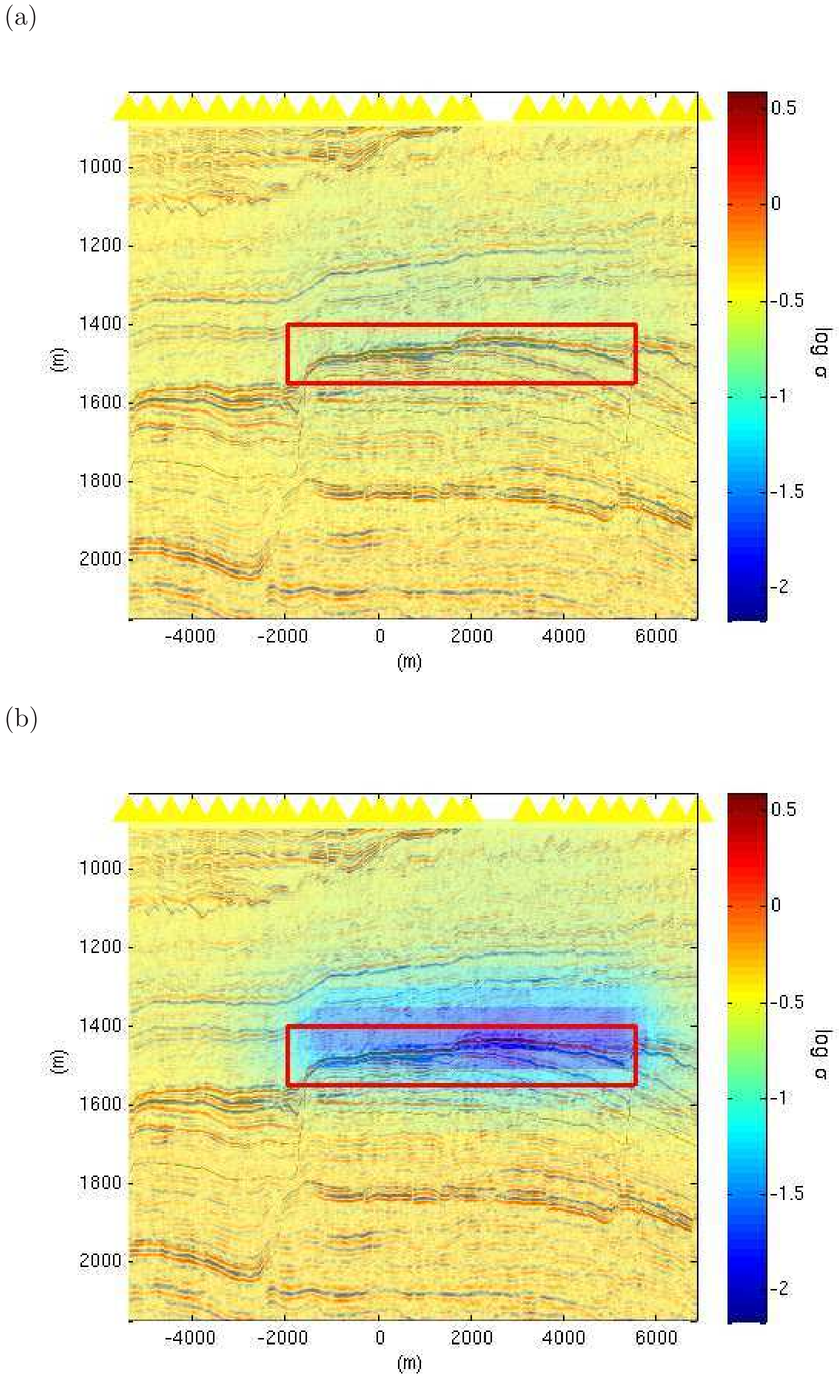

Figure 16: TIV inversion results for the 2003 Troll dataset laid over a seismic section. Triangles denote lateral receiver positions, red rectangle marks main reservoir. (a) σ_h, (b) σ_v.

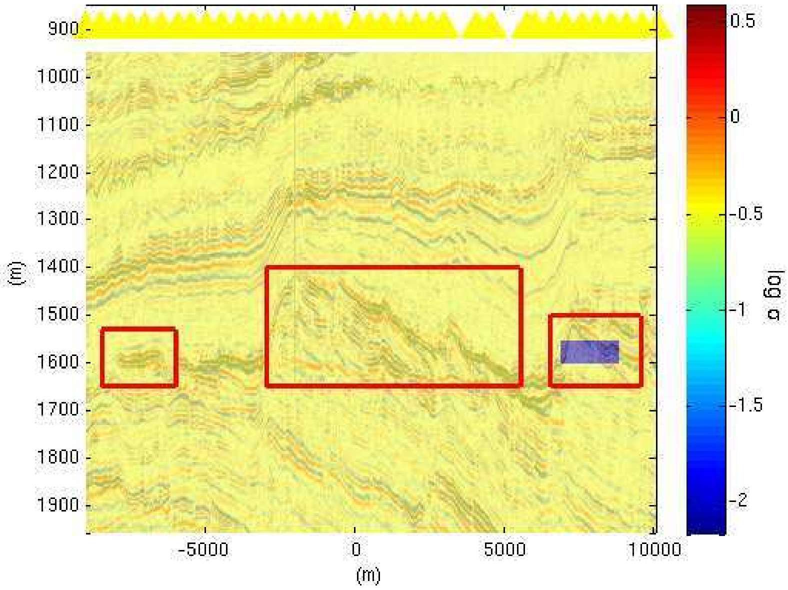

Figure 17: Initial model for the 2008 Troll dataset laid over a seismic section. Triangles denote lateral receiver positions, red rectangles mark reservoirs.

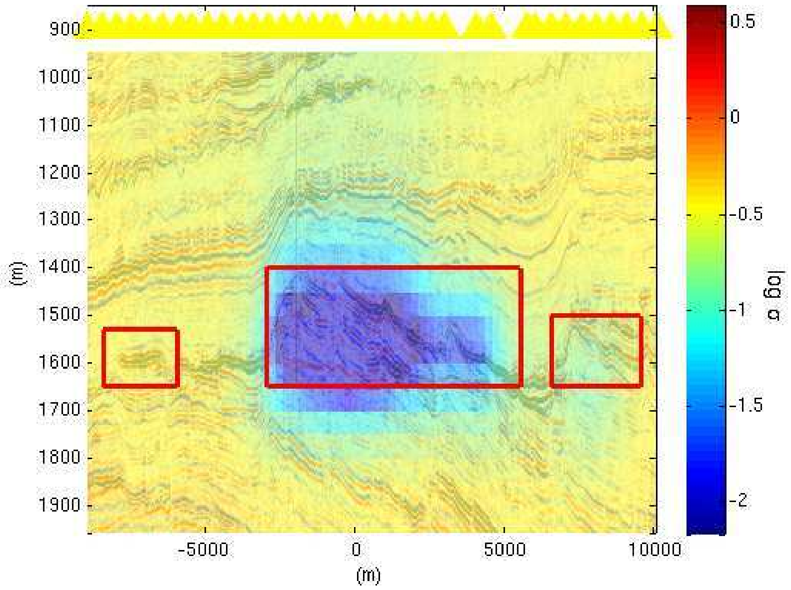

Figure 18: Isotropic inversion result for the 2008 Troll dataset laid over a seismic section. Triangles denote lateral receiver positions, red rectangles mark reservoirs.

(a)

(b)

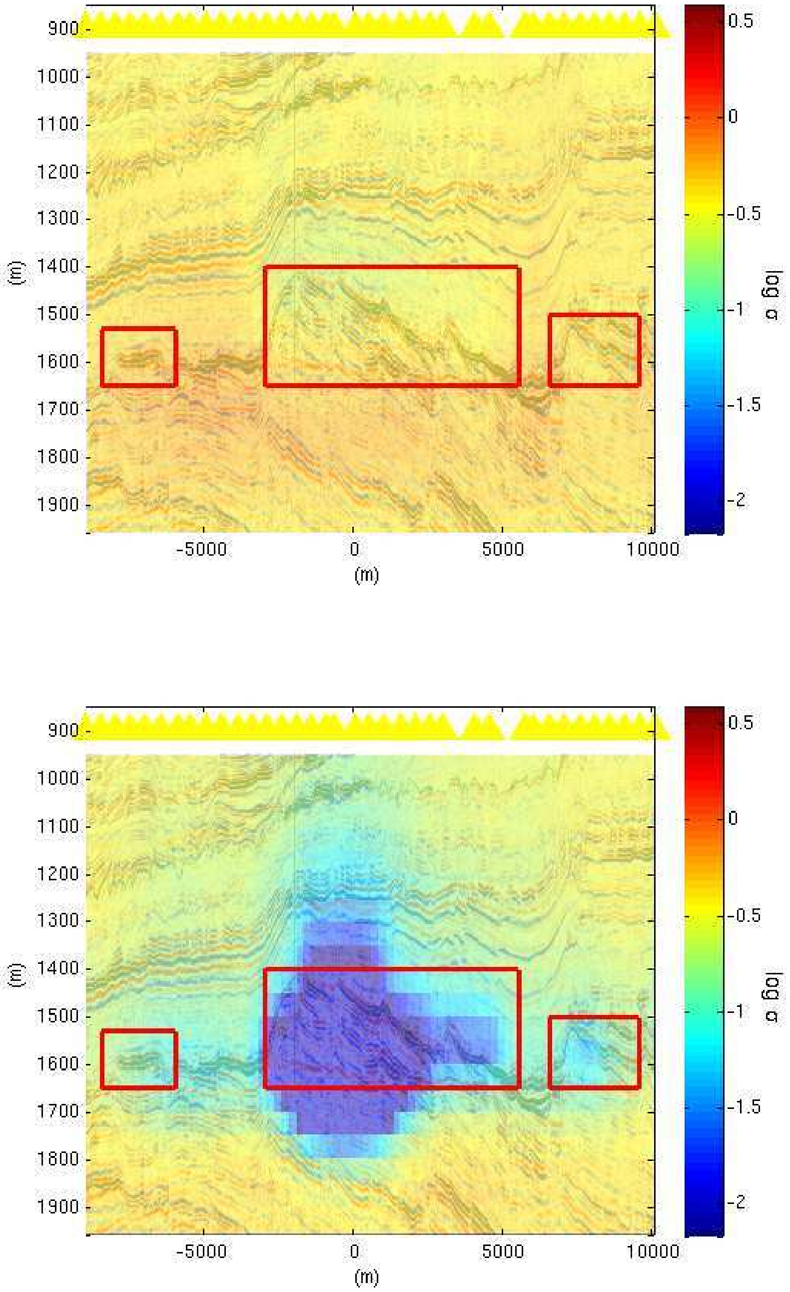

Figure 19: TIV inversion results for the 2008 Troll dataset laid over a seismic section. Triangles denote lateral receiver positions, red rectangles mark reservoirs. (a) σ_h, (b) σ_v.

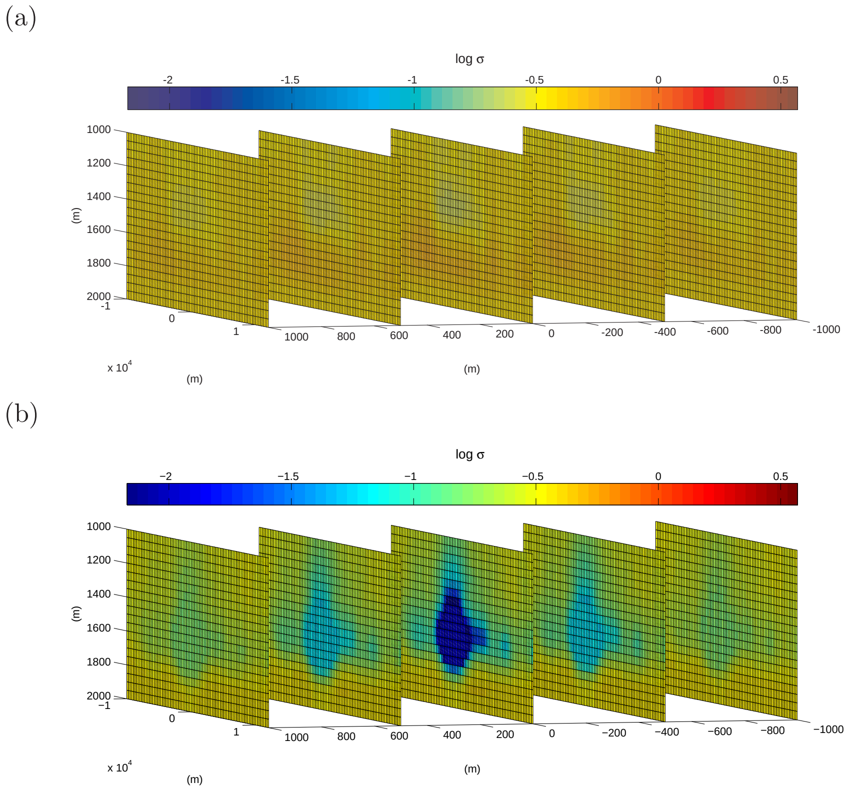

Figure 20: Slices orthogonal to the sailing line through reconstructed domain $\mathcal{D}$ showing TIV inversion results for the 2008 Troll dataset. (a) σ_h, (b) σ_v.

(a)

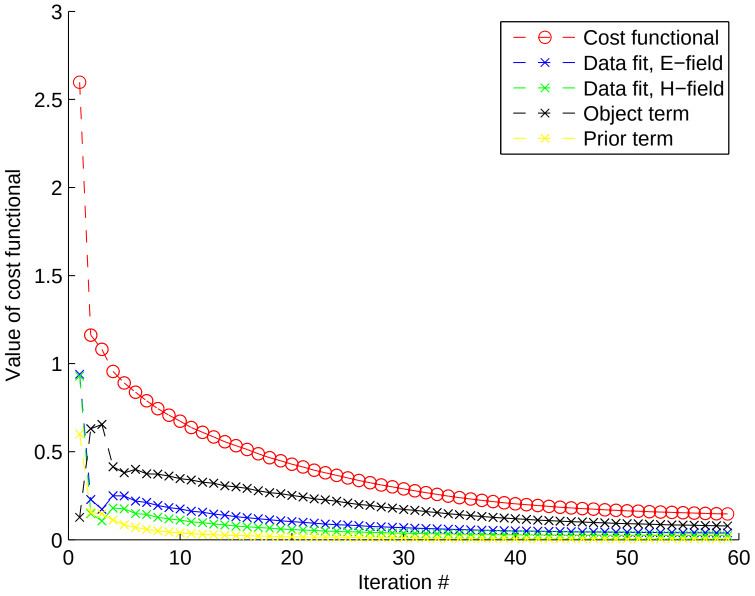

(b)

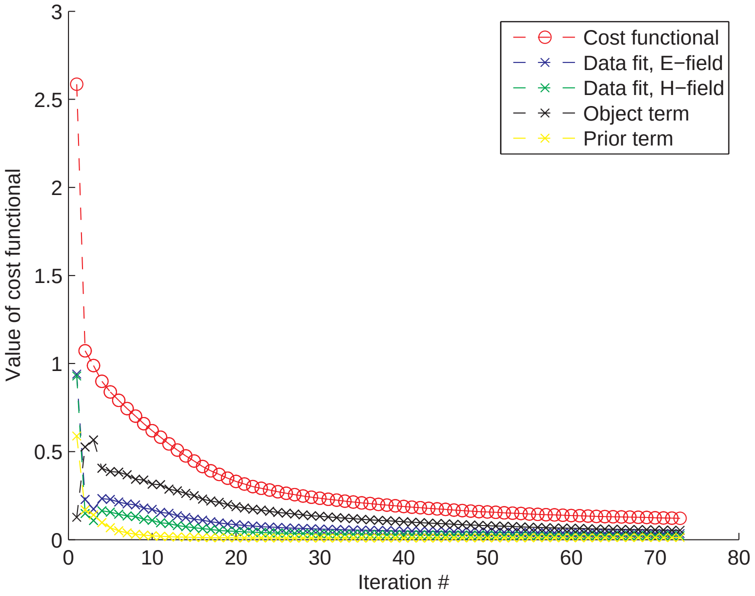

Figure 21: Convergence history for the Troll 2008 example. (a) Isotropic, (b) TIV.